NORMAL FORCE CALCULATIONS FOR ROCKET-LIKE CONFIGURATIONS

Enda Dimitri Vieira Bigarelli, João Luiz F. Azevedo
CTA/IAE/ASE-N – 12228-904 – São José dos Campos, SP, Brasil

Abstract

Transonic and supersonic flow simulations over typical launch vehicle configurations are presented. A 3-D finite difference numerical code, written for general, curvilinear, body-conforming coordinate systems, is used. The code solves the thin-layer approximation for the laminar Navier-Stokes equations. Simulations are performed for a launcher and a sounding rocket configurations, currently under development at IAE. Calculations consider cases at angle of attack and at various freestream Mach numbers. Normal force coefficients are obtained such that the loads required for the design phase can be determined. Computational results are compared to available experimental data. In general, good results within engineering error margins are obtained.

1 Introduction

Launch vehicles are typically designed to fly at very low angles of attack. Nevertheless, even at such low angles of attack, the lateral loads that arise in these vehicles are quite strong and they must be accurately determined. Therefore, during the design process, one is required to determine the aerodynamics of these vehicles at angle of attack because this will provide the loads required for the structural design of the vehicle as well as the flight dynamics stability characteristics necessary for the control system design. Earlier work [14, 3] has presented axisymmetric viscous simulations for flows over the VLS with

very good representation of the flow physics. Moreover, three-dimensional inviscid computations over the VLS at low angles of attack with good agreement with experimental data were also performed [2].

This earlier work, however, considered fairly simple 3-D geometries and, typically, mesh refinement was less than adequate due to computational resource limitations. This discussion emphasizes that the problem of simulating transonic and supersonic flows over complex vehicles is not a new requirement at IAE. However, recently, the development of the computational tools available in the CFD group [5], together with additional computational resources available in the country, have made possible the analysis of almost realistic configurations. In this context, Ref. [4] presented results for the complete, 1st-stage flight, VLS configuration. The comparisons included in that work considered solely flight conditions at zero angle of attack. The present work, despite the fact that it does not include the VLS lateral boosters in the configurations analysed, is aimed at studying the behaviour of running normal force coefficients and normal force coefficient slopes as a function of Mach number. These analyses are closer to the primary aerodynamic data the designer needs in order to asses structural loads and control system effectiveness. Moreover, they require the consideration of flight conditions at angle of attack.

Hence, the computational code is used to simulate the 3-D flows about two vehicles now under development at IAE, namely the first Brazilian Satellite Launch Vehicle (VLS) and the Sonda

III-A sounding rocket, at angle of attack and for various freestream Mach numbers. VLS is a four-stage satellite launcher built with four booster attached to a main body. In the present work, computations were performed considering only the vehicle central body. The solver used is a 3-D finite-difference code written for general, body-conforming, curvilinear coordinate systems and solves the thin-layer approximation of the compressible laminar Navier-Stokes equations.

It should be remarked that the correct representation of the flowfields of interest should consider a turbulent viscous formulation. Actual flight Reynolds numbers for the vehicles are very large, of the order of 10^7, and some relevant phenomena defining the flow topology require a viscous turbulent formulation. Nevertheless, this paper includes only laminar Navier-Stokes results, since it is an account of the evolutionary process towards the complete flow simulation capability desired. These results are necessary in order to address the level of accuracy that can be attained with the computational tool under development.

2 Theoretical Formulation

The numerical code used solves the thin-layer approximation of the 3-D, compressible, laminar Navier-Stokes equations. These equations can be written in strong conservation-law form for general, body-conforming, curvilinear coordinates [11], as

$$\frac{\partial \overline{Q}}{\partial \tau} + \frac{\partial \left(\overline{E} - \overline{E}_v \right)}{\partial \xi} + \frac{\partial \left(\overline{F} - \overline{F}_v \right)}{\partial \eta}$$
$$+ \frac{\partial \left(\overline{G} - \overline{G}_v \right)}{\partial \zeta} = 0 \,, \quad (1)$$

where the vector of conserved quantities, $\overline{Q}$, is defined as

$$\overline{Q} = J^{-1} \left[\begin{array}{ccccc} \rho & \rho u & \rho v & \rho w & e \end{array} \right]^{\mathrm{T}} . \quad (2)$$

The formulation for the inviscid flux vectors, $\overline{E}$, $\overline{F}$ and $\overline{G}$, and the viscous flux vectors, $\overline{E}_v$, $\overline{F}_v$ and $\overline{G}_v$, can be found in Ref. [7]. In the case of the viscous flux vectors, despite the inclusion of the viscous terms in the ξ and ζ directions, all cross derivative terms were not considered in this formulation. Moreover, the meshes used in the simulations do not give support to viscous dissipation in those directions, so that the formulation should be referred as a thin-layer model. The Reynolds number, based on the freestream speed of sound, a_∞, density, ρ_∞, viscosity, μ_∞, and vehicle diameter, d, is given as $Re = \rho_\infty a_\infty d / \mu_\infty$.

In the usual CFD nomenclature, adopted in the present work, ρ is the density, u, v and w are the Cartesian velocity components, p is the pressure and e is the total energy per unity of volume. The pressure is obtained from the equation of state for perfect gases. Throughout this work, the curvilinear coordinate system is defined such that ξ is the rocket longitudinal direction, positive downstream, η is the wall-normal direction, and ζ is the circumferential direction. Expressions for the Jacobian of the transformation, J, and for the various metric terms can be found in Ref. [11], among other references.

3 Numerical Implementation

The governing equations are discretized in a finite difference context. The spatial discretisation adopted uses a central difference algorithm plus explicitly added artificial dissipation terms in order to control nonlinear instabilities. The equations, fully discretised in space, can be written as

$$\left(\frac{\partial \overline{Q}}{\partial \tau} \right)_{i,j,k} = -\mathrm{RHS}_{i,j,k} \,. \quad (3)$$

The right-hand side operator of Eq. (3) is defined as

$$\mathrm{RHS}_{i,j,k} =$$
$$= \frac{\overline{E}_{i+1,j,k} - \overline{E}_{i-1,j,k}}{2\Delta\xi} - \frac{\overline{E}_{v_{i+\frac{1}{2},j,k}} - \overline{E}_{v_{i-\frac{1}{2},j,k}}}{\Delta\xi}$$
$$+ \frac{\overline{F}_{i,j+1,k} - \overline{F}_{i,j-1,k}}{2\Delta\eta} - \frac{\overline{F}_{v_{i,j+\frac{1}{2},k}} - \overline{F}_{v_{i,j-\frac{1}{2},k}}}{\Delta\eta}$$
$$+ \frac{\overline{G}_{i,j,k+1} - \overline{G}_{i,j,k-1}}{2\Delta\zeta} - \frac{\overline{G}_{v_{i,j,k+\frac{1}{2}}} - \overline{G}_{v_{i,j,k-\frac{1}{2}}}}{\Delta\zeta}$$
$$- \frac{J^{-1}_{i+\frac{1}{2},j,k} d_{i+\frac{1}{2},j,k} - J^{-1}_{i-\frac{1}{2},j,k} d_{i-\frac{1}{2},j,k}}{\Delta\xi}$$

$$- \frac{J^{-1}_{i,j+\frac{1}{2},k} d_{i,j+\frac{1}{2},k} - J^{-1}_{i,j-\frac{1}{2},k} d_{i,j-\frac{1}{2},k}}{\Delta\eta}$$

$$- \frac{J^{-1}_{i,j,k+\frac{1}{2}} d_{i,j,k+\frac{1}{2}} - J^{-1}_{i,j,k-\frac{1}{2}} d_{i,j,k-\frac{1}{2}}}{\Delta\zeta} , \qquad (4)$$

where $\Delta\xi = \Delta\eta = \Delta\zeta = 1$ for the general curvilinear coordinate case. An anisotropic scalar artificial dissipation method [13] was used. This scheme is nonlinear and allows a selection between artificial dissipation terms of second and fourth differences, which is very important in capturing shock waves in the flow. In Eq. 4, the artificial dissipation is represented by the d terms.

Time march uses an explicit, second order, five-stage Runge-Kutta scheme [8, 9], which can be written as

$$\begin{aligned}
\overline{Q}^{(0)}_{i,j,k} &= \overline{Q}^{n}_{i,j,k} , \\
\overline{Q}^{(\ell)}_{i,j,k} &= \overline{Q}^{(0)}_{i,j,k} - \alpha_\ell \Delta t_{i,j,k} \mathrm{RHS}^{(\ell-1)}_{i,j,k} , \quad (5) \\
\overline{Q}^{n+1}_{i,j,k} &= \overline{Q}^{(5)}_{i,j,k} ,
\end{aligned}$$

where $\ell = 1, 2, \ldots, 5$. Numerical values for the α_ℓ parameters can be found in [8]. In the previous expressions, Δt stands for the time step, and n and $n+1$ refer to the property values at the start and at the end of each time step, respectively. Equation (5) also indicates that a local time step option is being used in order to accelerate convergence to steady state calculations.

4 Boundary Conditions and Computational Grids

For the configurations of interest here, the types of boundary conditions that should be considered include solid wall, far field, symmetry, upstream centerline and downstream (exit) conditions. For the rocket wall, the velocity vector is set to zero, and a zero-th order extrapolation of the pressure and the density is performed. The upstream centerline is a singularity of the coordinate transformation and, hence, an adequate treatment of this boundary must be provided. In the present case, the approach consists in extrapolating the property values from the adjacent longitudinal plane and in averaging the extrapolated values in the

azimuthal direction in order to define the updated properties at the upstream centerline. At the exit plane, the boundary conditions are implemented through the use of the 1-D characteristic relations for the 3-D Euler equations. The interested reader is referred to Ref. [1] for further details on the use of 1-D characteristic relations for boundary condition implementation. Freestream properties are assumed at the far field boundaries.

Furthermore, in order to reduce computational costs, the grids used in the numerical simulations performed are generated for half a body in the azimuthal direction. This simplification is valid for the cases assessed in this work because low angles of attack are considered. This condition implies a symmetric flow about the pitching plane, as indicated in Ying (1986) among other references. Hence, symmetry is applied in the pitching plane using two auxiliary planes, namely, $k = 1$ and $k = kmax$. Those extra planes are added, respectively, before the leeside and after the windside pitching plane. The final grid for the VLS main body configuration to which numerical results are mesh independent had $156 \times 65 \times 21$ points. The computational mesh for the Sonda III-A configuration had the same number of points. A view of a longitudinal plane of these grids is shown in Fig. 1.

5 Pressure Coefficient Results

In this section, the numerical simulations of the flow over the VLS second stage flight configuration at freestream Mach numbers $M_\infty = 1.25$ and 3.00, and angles of attack $\alpha = 0$ and 4 deg. are presented. The computations are compared to available experimental data, obtained through wind tunnel tests. This comparison is necessary to assess the correctness of the numerical method developed such that it can be used to obtain aerodynamic data for vehicles to which no experimental data are available.

In general, good agreement between the numerical and the experimental results is obtained. The numerical curves are qualitatively similar to the experimental ones. It is shown in the forthcoming comparisons that shock wave and expan-
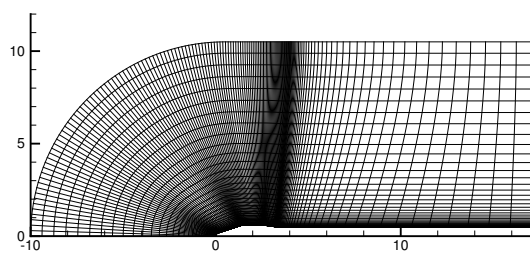
(a) VLS.
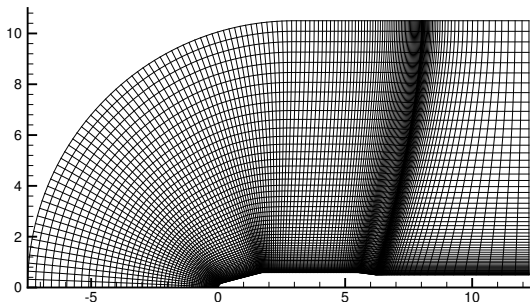
(b) Sonda III-A.

Fig. 1 Overall view of a plane from the 3-D grids used.

Fig. 2 Numerical Cp distributions compared to experimental data for the VLS central body at $\alpha = 0$ deg. and $M_\infty = 1.25$. Reynolds number is 30 million.

sion locations are well captured by the numerical procedure. Nevertheless, in some regions of the flow, computational simulations may not seem to be accurate when compared to wind tunnel results. This behaviour can be explained by the fact that, in those regions, turbulence and interactions between shock waves and boundary layer play a fundamental role in the flow configuration.

A comparison between the computational results and available experimental data can be seen in Fig. 2. Pressure coefficient, Cp, distributions for two different longitudinal rocket planes, which are the vehicle leeward and windward generators, are presented. This figure shows the results for the flow over the VLS central body at freestream conditions $\alpha = 0$ deg. and $M_\infty = 1.25$. These results indicate that the experimental data and the computational solution do not present large differences. In particular, the correct trends in the Cp distribution are captured by the numerical simulation. Several other similar com-
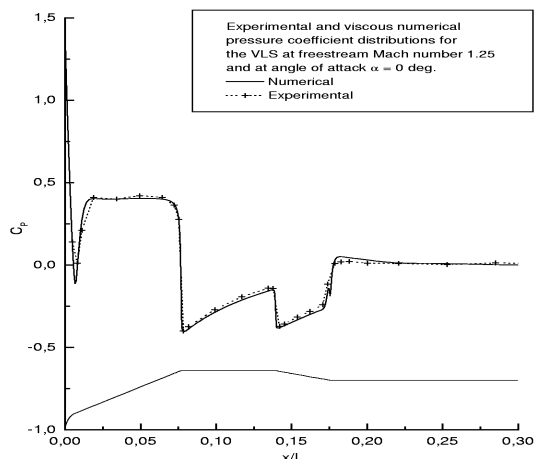
parisons, at different flight conditions, are available for flow simulation over the VLS. However, the comparison shown in Fig. 2 is representative of the level of agreement which can be obtained between the experimental data and the computational simulation results throughout the speed range analysed.

Similar Cp results for the VLS configuration at a higher freestream Mach number, namely $M_\infty = 3.00$, are shown in Fig. 3. This is a more demanding test case for the solver since, at this flight condition, strong shock waves are present in the flow. As in the previous case, the angle of attack is zero. Figure 4 shows Cp distributions over the VLS second stage flight configuration at an angle of attack $\alpha = 4$ deg. and freestream Mach number $M_\infty = 1.25$. Here, results are presented for the vehicle lee- and windside. In this case, since a positive angle of attack is considered, one can observe that the windside pressures are higher than the leeside ones, as expected. In general, one can observe in Fig. 4 that the agreement between numerical and experimental data is fairly good throughout the vehicle, except around the boattail-afterbody cylinder intersection. An interaction between shock wave and boundary layer exists in this region and this is of fundamental importance for the local flow configuration. However, the levels of approximation of the
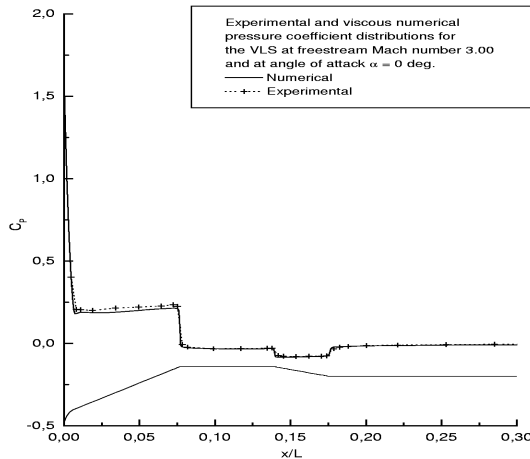
Fig. 3 Numerical *Cp* distributions compared to experimental data for the VLS central body at α = 0 deg. and $M_\infty = 3.00$. Reynolds number is 30 million.

Fig. 4 Numerical *Cp* distributions compared to experimental data for the VLS central body at α = 4 deg. and $M_\infty = 1.25$. Reynolds number is 30 million.

formulation used in the numerical code presented here are not yet detailed enough to represent this interaction correctly. Similar distributions for the VLS central body at a higher freestream Mach number, namely $M_\infty = 3.00$, are presented in Fig. 5. As in the previous case, the angle of attack is α = 4 deg. and the *Cp* distributions are presented for the vehicle lee- and windside planes.

One can observe that numerical results are much alike the experimental ones, despite that an efficient turbulent model should be added to the code in order to correctly simulate flow phenomena in certain regions. However, as stated before, this work is an evolutionary step towards a more general simulation capability. The group has already initiated some tests with single- and two-equation turbulence models, namely the Spalart-Allmaras [12] and the Menter SST [10] turbulence closures, with good results so far.

6 Normal Force Coefficient Results

For actual applications in design, one is typically concerned with the running normal loads and not with the local pressure distributions. Hence, circumferential integrations of the pressure coefficient distributions were performed to obtain the running normal force coefficients. These normal forces are calculated for different angles of attack
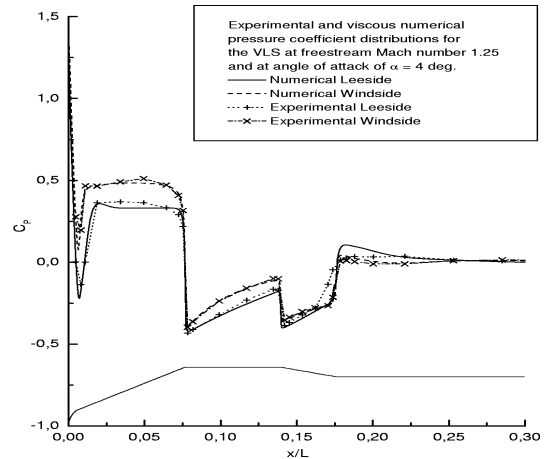
such that the normal force coefficient slope can also be obtained. Further details on the procedure adopted for calculation of the normal force coefficients can be seen in Ref. [7]. One should observe that several other vehicles are currently being developed, or improved, within the range of responsibilities of IAE. Due to budgetary constraint in the country, it is not always possible to take these other vehicles to the wind tunnel, especially because this typically means performing tests overseas. The approach which is currently being pursued is to use the experimental data available for the VLS to validate computational tools currently under development. Hence, this flow simulation capability can be applied to the other vehicles of interest, since the overall configurations are not that different from the VLS central body. One of such derivative vehicles is the Sonda III-A [7], which is a modified version of an existing sounding rocket. The normal force results obtained for the Sonda III-A under the present effort are being used for actual design work without experimental verification.

6.1 VLS Results

In this section, the running normal force coefficient distributions for the flow over the VLS second stage flight condition at freestream Mach
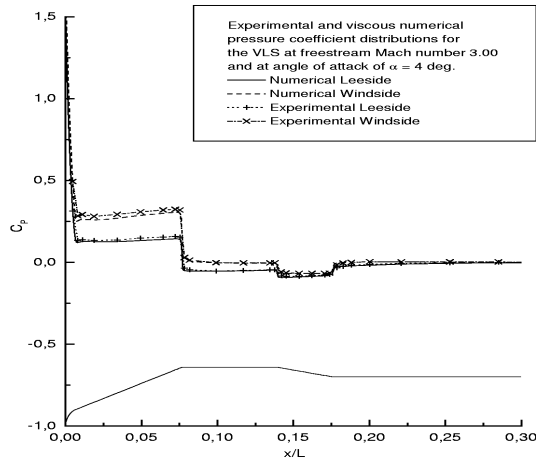
Fig. 5 Numerical Cp distributions compared to experimental data for the VLS central body at $\alpha = 4$ deg. and $M_\infty = 3.00$. Reynolds number is 30 million.

Fig. 6 Running normal force coefficients obtained with the viscous formulation compared to experimental data for the VLS central body at $M_\infty = 1.25$, $Re = 30$ million and at two different angles of attack.

numbers $M_\infty = 0.90$, 1.25, 2.00 and 3.00, and angles of attack $\alpha = 2$ and 4 deg. are presented. The normal force distribution, dC_N/dx, for the VLS central body at a freestream Mach number $M_\infty = 1.25$ is seen in Fig. 6. This figure presents the computational results compared to the experimental data for two different angles of attack, namely $\alpha = 2$ and 4 deg. Numerical and experimental curves are qualitatively alike, except for the boattail region. As previously mentioned, aerodynamics in this region is very dependent on turbulent flow phenomena, such as boundary layer separation due to adverse pressure gradient and interactions between shock wave and boundary layer. Hence, it is expected that the level of approximation of the governing equations used in this work is not able to correctly simulate the exact flow behaviour.

Figure 7 shows similar results for the VLS at higher freestream Mach numbers. Flight conditions considered were freestream Mach number $M_\infty = 2.00$ and angles of attack $\alpha = 2$ and 4 deg. One can verify that experimental and numerical curves are qualitatively similar to each other. However, in this case, it is possible to observe that there is a larger difference between computational and experimental data. This difference in the normal force coefficient distribution can be as large as 25% at some longitudinal stations
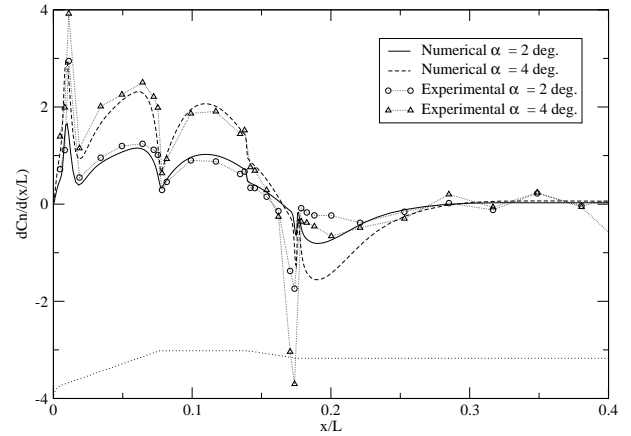
along the VLS central body. At this point in time, there is not a satisfying explanation for this result. Furthermore, since these differences are considerably larger in this case, additional numerical studies are currently under way in order to try to further assess the correctness of the computations for this $M_\infty = 2.00$ case results.

Running normal loads were also calculated for the vehicle at freestream Mach number $M_\infty = 3.00$ and at the same angles of attack as in the previous cases. One can see a comparison between numerical and experimental results in Fig. 8. This case has stronger shock waves present in the flow and, hence, it is a more challenging test case for the numerical code. One can observe, however, that the features of the flow are well captured by the code. Another highly demanding test case is a transonic flight condition. Running normal force loads were obtained for the VLS at freestream Mach number $M_\infty = 0.90$ and angles of attack $\alpha = 2$ and 4 deg. Numerical and experimental results for this simulation are presented in Fig. 9. In this case, a strong shock wave builds up over the payload fairing region and it is not attached to any geometric discontinuity. Large differences between computational and experimental data can be observed in Fig. 9. This is another example of the influence of the boundary layer-shock wave interaction in the flow config-
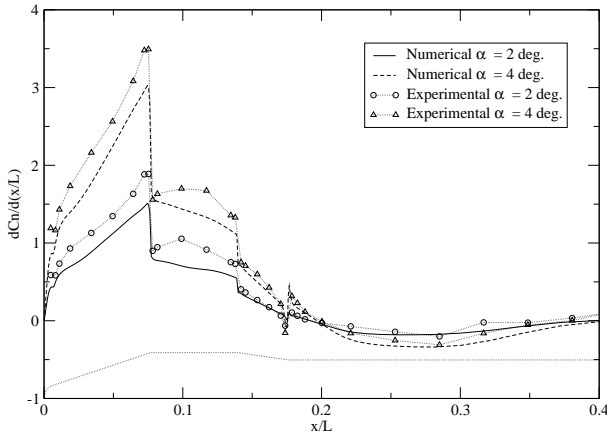
6

Fig. 7 Running normal force coefficients obtained with the viscous formulation compared to experimental data for the VLS central body at $M_\infty = 2.00$, $Re = 30$ million and at two different angles of attack.

Fig. 8 Running normal force coefficients obtained with the viscous formulation compared to experimental data for the VLS central body at $M_\infty = 3.00$, $Re = 30$ million, and at two different angles of attack.

uration. Preliminary turbulent results are already available for this flow condition and show much better agreement with experimental data [6].

The running normal force coefficient slope is obtained as the slope of dC_N/dx vs. α at a given crossflow plane. Since this work deals with small angles of attack, the slope for a given section is approximated by the slope of the best linear-fit curve throughout the set of three points, one point for each angle of attack. Figure 10 presents numerical and experimental results concerning the running normal force coefficient slopes over the VLS central body. Freestream Mach numbers considered were $M_\infty = 1.25$, 2.00 and 3.00. It can be observed in this figure that both numerical and experimental curves are qualitatively alike. This behaviour is to be expected since these normal force slopes are derived from the same normal force coefficients already presented here for the VLS configuration. Furthermore, the good agreement observed for $M_\infty = 2.00$ is a good indication that the numerical code is capturing the correct trends in the vehicle normal load slopes, even though the agreement of the actual running loads for this Mach number was not good, as indicated in Fig. 7.

The running normal force coefficient distributions can be integrated along the vehicle wall, resulting in the integrated normal force coeffi-
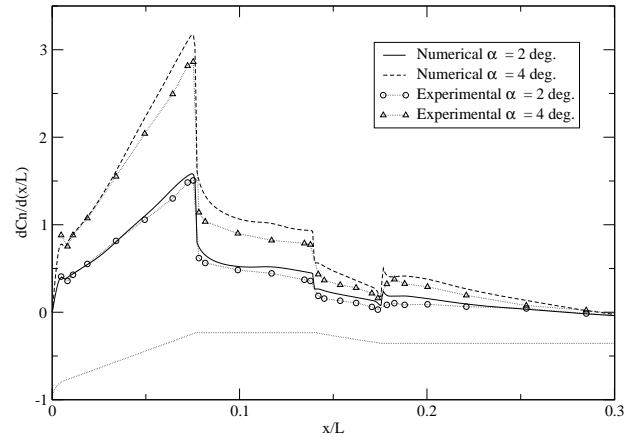
cient. This information is important to the design process as well as the running normal force distributions. Table 1 presents numerical and experimental integrated normal force coefficients. Obviously, a zero angle-of-attack condition yields zero normal force coefficients due to the flow symmetry. It can be observed that numerical values are smaller than the experimental ones. One can verify that the differences are usually of the order of 10% for the majority of the cases analysed. Nevertheless, as already discussed, the results for freestream Mach number $M_\infty = 2.00$ have a poorer correlation. Discrepancies for this Mach number are of the order of 25% for the $\alpha = 2$ deg. case and 17% for the $\alpha = 4$ deg. case. It should be observed that errors of about 10% can certainly be considered within the limitations of the level of approximation of the numerical formulation.

6.2 Sonda III-A Results

In a very similar way as described for the VLS case, the running normal force coefficients over the Sonda III-A were also calculated. The running normal force coefficient distributions were integrated along the vehicle wall, resulting in the integrated normal force coefficient. Table 2 presents the numerical integrated normal force

Table 1 Numerical and experimental integrated normal force coefficients, C_N, and normal force coefficient slopes, C_{N_α}, for the VLS central body.

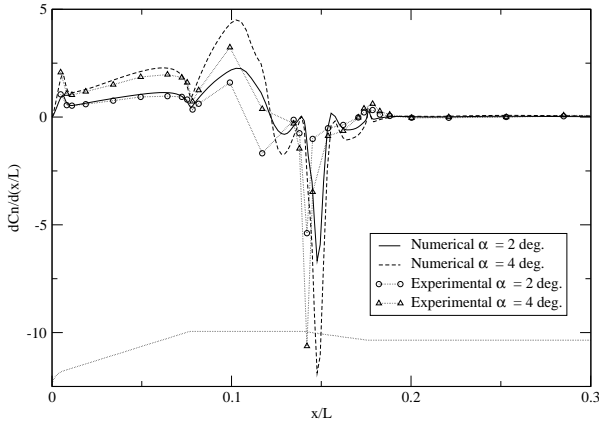| M_∞	C_N				C_{N_α} (1/deg.)	
	$\alpha = 2$ deg.		$\alpha = 4$ deg.			
	Num.	Exp.	Num.	Exp.	Num.	Exp.
1.25	0.0880	0.0937	0.1782	0.1928	0.0430	0.0467
2.00	0.1075	0.1424	0.2216	0.2652	0.0554	0.0607
3.00	0.1189	0.1321	0.2473	0.2793	0.0618	0.0710

Fig. 9 Running normal force coefficients obtained with the viscous formulation compared to experimental data for the VLS central body at $M_\infty = 0.90$, $Re = 25$ million, and at two different angles of attack.

Fig. 10 Numerical and experimental normal force slopes for the VLS at freestream Mach numbers $M_\infty = 1.25$, 2.00 and 3.00.

coefficients. As stated before, the zero angle-of-attack flight condition yields zero normal force coefficients, due to the flow symmetry. As stated before, these results were actually used for the vehicle design.

7   Concluding Remarks

This work presents the application of the capability implemented at IAE to solve three-dimensional flows over complex aerospace configurations at angle of attack to determine important aerodynamic loads required at the design stage. A computational code which solves the 3-D, compressible thin-layer approximation of the laminar compressible Navier-Stokes equations for general, body-conforming, curvilinear
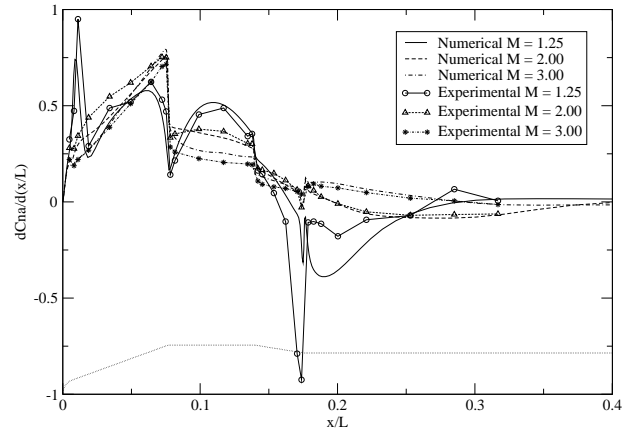
coordinates was developed. The numerical code was used to simulate flows about the VLS central body and the Sonda III-A configuration at freestream Mach numbers of 0.90, 1.25, 2.00 and 3.00, and angles of attack of 0, 2 and 4 deg.

Some validation analyses involved the comparison of computational results to available experimental data for the VLS main body configuration. In general, good agreement between the numerical and the experimental results was obtained. Nevertheless, in some regions of the flow, computational simulations were not able to capture the exact flow behaviour. This can be explained by the fact that, in those regions, turbulence and interactions between shock waves and boundary layer are determinant for the flow configuration.

Some numerical results were presented for a configuration to which there are no available ex-

Table 2 Integrated normal force coefficients, C_N, and normal force coefficient slopes, C_{N_α}, for the Sonda III-A.

M_∞	C_N $\alpha = 2$ deg.	C_N $\alpha = 4$ deg.	C_{N_α} (1/deg.)
1.25	0.0886	0.1775	0.0444
2.00	0.0875	0.1856	0.0464
3.00	0.0906	0.1974	0.0494

perimental data, due to budgetary constraints in the country. Considering the good agreement, i.e., within engineering error margins, obtained for the VLS case, the computational results for flows over the Sonda III-A could be used directly to the vehicle design stage.

Finally, it can be stated that the correct representation of the flowfields of interest requires a turbulent viscous formulation. Nevertheless, only laminar Navier-Stokes results are considered because this work is an account of the evolutionary process towards the complete flow simulation capability desired. These results are necessary in order to address the level of accuracy that can be attained with the computational tool under development. The CFD group at IAE is already working to implement turbulence models into this code. This will be an important step aiming at the broadening of the Institute simulation capability.

Acknowledgements

References

[1] Azevedo J. L. F, Fico Jr. N. G. C. R, and Ortega M. A. Two-dimensional and axisymmetric nozzle flow computations using the Euler equations. *Journal of the Brazilian Society of Mechanical Sciences*, Vol. 17, No 2, pp 147–170, 1995.

[2] Azevedo J. L. F, Moraes Jr. P, Maliska C. R, Marchi C. H, and Silva A. F. C. Code validation for high-speed flow simulation over satellite launch vehicle. *Journal of Spacecraft and Rockets*, Vol. 33, No 1, pp 15–21, 1996.

[3] Azevedo J. L. F, Zdravistch F, and Silva A. F. C. Implementation and validation of Euler solvers for launch vehicle flows. *Proc 4th International Symposium on Computational Fluid Dynamics*, pp 42–47, Davis, CA, USA, 1991.

[4] Basso E, Antunes A. P, and Azevedo J. L. F. A realistic application of computational fluid dynamics for the VLS project. *Proc 21st Iberian Latin American Congress on Computational Methods in Engineering – CILAMCE 2000*, Rio de Janeiro, RJ, Brazil, 2000.

[5] Basso E, Antunes A. P, and Azevedo J. L. F. Three dimensional flow simulations over a complete satellite launcher with a cluster configuration. *Proc 18th AIAA Applied Aerodynamics Conference and Exhibit*, pp 805–813, Denver, CO, USA, 2000.

[6] Bigarelli E. D. V and Azevedo J. L. F. On turbulence models for 3-D aerospace applications. *Proc 9th Brazilian Congress of Engineering and Thermal Sciences – ENCIT 02*, 2002. (to be presented).

[7] Bigarelli E. D. V, Mello O. A. F, and Azevedo J. L. F. Three dimensional flow simulations for typical launch vehicles at angle of attack. *Proc 15th Brazilian Congress of Mechanical Engineering – COBEM 99*, 1999.

[8] Jameson A and Mavriplis D. Finite volume solution of the two-dimensional Euler equations on a regular triangular mesh. *AIAA Journal*, Vol. 24, No 4, pp 611–618, 1986.

[9] Jameson A, Schmidt W, and Turkel E. Numerical solution of the Euler equations by finite volume methods using Runge-Kutta time-stepping schemes. *Proc AIAA 14th Fluid and Plasma Dynamics Conference*, Palo Alto, CA, USA, 1981.

[10] Menter F. R. Zonal two equation $k-\omega$ turbulence models for aerodynamic flows. *AIAA 24th Fluid Dynamics Conference*, pp 1–20, 1993.

[11] Pulliam T. H and Steger J. L. Implicit finite-difference simulations of three-dimensional compressible flow. *AIAA Journal*, Vol. 18, No 2, pp 159–167, 1980.

[12] Spalart P. R and Allmaras S. R. A one-equation turbulence model for aerodynamic flow. *La Recherche Aeropastiale*, Vol. 1, pp 5–21, 1994.

[13] Turkel E and Vatsa V. N. Effect of artificial viscosity on three-dimensional flow solutions. *AIAA Journal*, Vol. 32, No 1, pp 39–45, 1994.

[14] Zdravistch F and Azevedo J. L. F. Numerical simulation of high speed flows over complex satellite launchers. *Proc 3rd Brazilian Thermal Sciences Meeting – ENCIT 90*, pp 233–238, Itapema, SC, Brazil, 1990.